

Contents lists available at ScienceDirect

Journal of Energy Chemistry



journal homepage: www.elsevier.com/locate/jechem

Dedicated to the 100th anniversary of Chemistry at Nankai University

Single-atom catalysts with anionic metal centers: Promising electrocatalysts for the oxygen reduction reaction and beyond

Jinxing Gu^a, Yinghe Zhao^a, Shiru Lin^a, Jingsong Huang^{b,*}, Carlos R. Cabrera^c, Bobby G. Sumpter^b, Zhongfang Chen^{a,*}

- ^a Department of Chemistry, University of Puerto Rico, Rio Piedras Campus, San Juan, Puerto Rico 00931, USA
- ^b Center for Nanophase Materials Sciences, Oak Ridge National Laboratory, Oak Ridge, Tennessee 37831, USA
- ^c Department of Chemistry and Biochemistry, The University of Texas at El Paso, El Paso, Texas 79968, USA

ARTICLE INFO

Article history: Received 22 April 2021 Revised 2 August 2021 Accepted 5 August 2021 Available online 14 August 2021

Keywords: Single-atom catalysts Anionic metal centers Antimonene Oxygen reduction reaction Nitrogen reduction reaction

ABSTRACT

Ongoing efforts to develop single-atom catalysts (SACs) for the oxygen reduction reaction (ORR) typically focus on SACs with cationic metal centers, while SACs with anionic metal centers (anionic SACs) have been generally neglected. However, anionic SACs may offer excellent active sites for ORR, since anionic metal centers could facilitate the activation of O_2 by back donating electrons to the antibonding orbitals of O_2 . In this work, we propose a simple guideline for designing anionic SACs: the metal centers should have larger electronegativity than the surrounding atoms in the substrate on which the metal atoms are supported. By means of density functional theory (DFT) simulations, we identified 13 anionic metal centers (Co, Ni, Cu, Ru, Rh, Pd, Ag, Re, Os, Ir, Pt, Au, and Hg) dispersed on pristine or defective antimonene substrates as new anionic SACs, among which anionic Au and Co metal centers exhibit limiting potentials comparable to, or even better than, conventional Pt-based catalysts towards ORR. We also found that anionic Os and Re metal centers on the defective antimonene can electrochemically catalyze the nitrogen reduction reaction (NRR) with a limiting potential close to that of stepped Ru(0001). Overall, our work shows promise towards the rational design of anionic SACs and their utility for applications as electrocatalysts for ORR and other important electrochemical reactions.

© 2021 Science Press and Dalian Institute of Chemical Physics, Chinese Academy of Sciences. Published by ELSEVIER B.V. and Science Press. All rights reserved.

1. Introduction

Since the consumption of non-renewable fossil fuels has caused severe environmental problems such as air pollution and climate change, the sustainable development of human society demands clean, renewable, and high-capacity energy conversion/storage technologies [1,2]. Fuel cells are a very promising technology to meet the demand due to high efficiency and the zero emission of greenhouse gases [3,4]. However, the large-scale application of fuel cells is currently still hindered by the limited options of high-performance electrocatalysts for the oxygen reduction reaction (ORR) at the cathode [5–7]. To overcome this hindrance, a key challenge is to develop highly active, durable, and low-cost electrocatalysts [8,9]. To date, platinum group metals (PGM) are the most efficient electrocatalysts for ORR, but their high costs urge researchers to develop viable alternatives with lower PGM loading

 $\hbox{\it E-mail addresses: $huangj3@ornl.gov (J. Huang), $zhongfangchen@gmail.com (Z. Chen).}$

and even PGM-free electrocatalysts [10–17]. Among strategies to reduce the loading of noble metals or even replace them with non-precious metals [18,19], developing single-atom catalysts (SACs) with atomically dispersed active metal centers is very encouraging [20,21].

SACs have been widely applied as catalysts for various electrochemical reactions (such as oxygen evolution reaction, nitrogen reduction reaction, and CO₂ reduction reaction), methane activation, water gas shift reaction, and hydrogenation reactions [22–24]. Compared with the bulk counterparts, SACs not only greatly maximize the utilization of metals, but also exhibit extraordinary activities and stabilities [25–31]. Moreover, the catalytic performance of SACs could be rationally improved, because the single-atom centers and their well-defined chemical environment provide an excellent test ground to reveal the relationship between the catalytic performance and the catalyst structures at the atomic level. A potential approach to tweak the performance of SACs is to modify the charge state of the metal centers [32,33]. For example, Han et al. successfully doped sulfur atoms in the carbon matrix of the Fe-N-C SAC and attached one chlorine atom directly to the Fe

^{*} Corresponding authors.

center. The Fe-Cl near-range interaction and the Fe-S long-range interaction ensure the Fe center with a moderate positive charge state, resulting in a high half-wave potential (0.921 V) for ORR, which far exceeds that of commercial Pt/C catalyst in the alkaline solution (0.842 V) [34].

Typically, active sites of SACs for ORR carry positive charges [34]. However, anionic metal centers, which were unveiled decades ago [35-42], may also serve as active sites towards ORR. In Pt-M alloy nanoparticles (M = Mn, Fe, Co, Ni, Pd) [43-49], for instance, the negatively charged Pt atom can favorably transfer excess electrons to the antibonding orbitals of O2 molecule, thereby weakening the O-O bond and facilitating the electrochemical reduction of oxygen [46,49]. It is noteworthy that Pt-Ni bimetallic octahedra exhibit a much-enhanced ORR specific activity that is 51-fold higher than the state-of-art Pt/C electrocatalyst [50]. Hence, an interesting question arises naturally: can we develop effective SACs for the ORR with anionic metal centers? It is highly worth exploring such anionic SACs because they inherit the advantage of average SACs to maximally utilize metal atoms and simultaneously benefit from the electron transfer capability of active anionic metal centers to facilitate the electrochemical reduction of O₂.

To realize anionic SACs, it is important to tune the "strong metal-support interaction" by selecting a proper substrate [25,51–53]. Herein we proposed a simple guideline: the metal centers should have larger electronegativity than their neighboring atoms in the substrate. To validate this guideline, we chose the recently synthesized antimonene as the substrate [54–58], because the electronegativity of Sb is smaller than many transition metals [59,60], and the high stability of antimonene makes it wellsuited for electrochemical applications under a wide pH range [61-64]. According to electronegativity on the Pauling scale, 16 transition metal atoms were first selected to disperse on the pristine (p-) and defective (d-) antimonene, all showing favorable binding energies. Then by density functional theory (DFT) calculations, we confirmed that 13 transition metal atoms are of anionic charge states. Especially, d-Au and p-Co were found to show high limiting potentials towards ORR. We further showed that anionic d-Os and d-Re can facilitate nitrogen reduction reaction. This work proposes a simple principle for designing anionic SACs and demonstrates the capability of these overlooked but important SACs for electrochemical applications.

2. Computational methods

Spin-polarized density functional theory (DFT) simulations were carried out with the Vienna ab initio simulation package (VASP) [65,66]. Geometry optimizations and electronic property calculations were performed using the Perdew-Burke-Ernzerhof (PBE) functional [67]. The interaction between ions and electrons was described with the projector augmented wave method [68,69]. A kinetic energy cutoff for plane waves was set to 450 eV. Structural relaxations used a conjugate gradient scheme without symmetry restrictions until the energy change in electronic iterations was smaller than 1×10^{-5} eV and the maximum force on each atom was less than 0.02 eV $Å^{-1}$. To avoid interactions between periodic images of active site, the vacuum space between surfaces was set as 20 Å in the vertical direction, and the supercell was modeled with lattice constants (a and b) larger than 10 Å in the lateral directions. The Brillouin zone was sampled by $3\times3\times1$ k-points grid using the Monkhorst-Pack scheme during geometry optimizations, while a denser k-points grid of $9\times9\times1$ was used for electronic property calculations [70]. The stability of SACs was evaluated by the binding energy (E_b) , which is defined as $E_b = E_{SAC} - E_{antimonene} - E_{TM}$, where E_{SAC} , $E_{antimonene}$, and E_{TM} are

energies of SACs, pristine or defective antimonene, and isolated transition metal atoms, respectively. Here, isolated atoms instead of bulk metals were used as the reference for binding energy calculations since SACs can be fabricated by means of chemical vapor deposition [71–76]. To better describe the adsorption of reaction intermediates on catalysts, Grimme's DFT-D3 method was employed to correct the van der Waals (vdW) interactions [77]. Stabilization effects of solvent on the intermediates were also considered using the algorithm as implemented in VASPsol package [78,79].

For electrochemical ORR in acidic media, the associative reaction pathway can be explained using a four-electron mechanism:

$$O_2(g) + *=*O_2$$
 (1a)

$$^*O_2 + H^+ + e^- = ^*OOH$$
 (1b)

$$*OOH + H^{+} + e^{-} = *O + H_{2}O(1)$$
 (1c)

$$^*O + H^+ + e^- = ^*OH$$
 (1d)

$$^{*}OH + H^{+} + e^{-} = ^{*} + H_{2}O(1)$$
 (1e)

where * denotes the catalyst, while * O_2 , *OOH, *O, and *OH are the oxygen-containing intermediates. Based on computational hydrogen electrode (CHE) model [80], the reaction Gibbs free energy change (ΔG) for each reaction step of Eq. (1) can be evaluated by adsorption free energies, shown as follows [81]:

$$\Delta G(1a) = \Delta G(^*O_2) - 4.92 \text{ eV}$$
 (2a)

$$\Delta G(1b) = \Delta G(^*OOH) - \Delta G(^*O_2) + eU_b$$
(2b)

$$\Delta G(1c) = \Delta G(^*O) - \Delta G(^*OOH) + eU_c$$
(2c)

$$\Delta G(1d) = \Delta G(^*OH) - \Delta G(^*O) + eU_d \eqno(2d)$$

$$\Delta G(1e) = -\Delta G(^*OH) + eU_e \tag{2e}$$

where the term U_i (i = b, c, d, and e) is the external potential on the electrode. When setting the ΔG for each reaction step in Eqs. (2b-2e) to 0, the equilibrium potentials for these steps (U_i^0) were obtained as follows:

$$U_{\rm b}^{0} = \Delta G(^{*}O_{2})/e - \Delta G(^{*}OOH)/e$$
 (3a)

$$U_c^0 = \Delta G(^*OOH)/e - \Delta G(^*O)/e \tag{3b}$$

$$U_d^0 = \Delta G(^*O)/e - \Delta G(^*OH)/e \tag{3c}$$

$$U_e^0 = \Delta G(^*OH)/e \tag{3d}$$

Theoretically, the catalytic performance for an electrocatalyst can be evaluated by the limiting potential, U_L , which is determined as min (U_i^0) [8,82]. For ORR, a higher U_L value corresponds to a lower overpotential (1.23 V – U_L), thus, indicating a better energy efficiency.

Adsorption free energies of intermediates, i.e., $\Delta G(^*O_2)$, $\Delta G(^*OOH)$, $\Delta G(^*O)$, and $\Delta G(^*OH)$ in Eqs. 2 and 3, were calculated based on the free energies of H_2O molecule in liquid phase and H_2 molecule in gas phase as follows:

$$xH_2O(l) + {}^* = {}^*O_xH_y + \frac{1}{2}(2x - y)H_2(g) \tag{4a}$$

$$\begin{split} \Delta G\big(^*O_xH_y\big) &= G\big(^*O_xH_y\big) + \frac{1}{2}(2x-y)G(H_2(g)) - xG(H_2O) \\ &- G(^*) \end{split} \tag{4b}$$

where *O_xH_y represents *O_2 , *OOH , *O , and *OH , depending on x and y values. Free energy G for each species is $G = E + G_{\text{correction}}$, where E is the total energy calculated from DFT simulations, and $G_{\text{correction}}$ is the correction term. For $H_2O(1)$ and $H_2(g)$, $G_{\text{correction}} = E_{ZPE} - TS$, where E_{ZPE} is the zero-point energy and S is the entropy, both taken from the NIST database and T was set to 298.15 K [83]. For *O_2 , *OOH , *O , and *OH , $G_{\text{correction}}$ was obtained with the aid of VASPKIT [84], where frequencies under 50 cm $^{-1}$ were set to 50 cm $^{-1}$. The E_{ZPE} , TS, and $G_{\text{correction}}$ for free molecules and intermediates are listed in Tables S1-S3. The Gibbs free energy of the O_2 molecule was derived as $G(O_2(g)) = 2G(H_2O(1)) - 2G(H_2(g)) + 4.92$ eV [80].

For the nitrogen reduction reaction (NRR), calculations involved structural optimizations of catalysts and intermediates (Scheme S1), the correction of free energy, and the determination of limiting potential. Details of these computations are deposited in the Supplementary Information.

3. Results and discussion

3.1. Antimonene-based anionic SACs

We selected antimonene as the substrate for SACs since the electronegativity of Sb is smaller than many transition metals. Antimonene features a buckled honeycomb geometry and consists of two sublayers of Sb atoms. The pristine antimonene has three possible sites (labeled as A, B, and C) for the adsorption of one transition metal atom, i.e., the site directly above the Sb atom in the lower sublayer, the site over the buckled hexagonal ring, and the site inside the buckled hexagonal ring, respectively (Fig. 1a). In the case of antimonene with a single-Sb vacancy, the transition metal atom can occupy the vacancy which is labeled as site D (Fig. 1a). For simplicity, structures with transition metals on the pristine antimonene are termed as p-M, while those with transition metals on the defective antimonene are termed as d-M.

To generate anionic SACs for study, we used electronegativity (χ) of Pauling scale to choose potential transition metals. As the χ of Sb is 2.05, transition metals with χ greater than 2.05 could obtain electrons from antimonene, forming negative charge states and anionic SACs. To allow some leeway for Sb's electronegativity, the cutoff value of χ was set as 1.80, following which 16 3d/4d/5d transition metal atoms (Fe, Co, Ni, Cu, Mo, Ru, Rh, Pd, Ag, W, Re, Os, Ir, Pt, Au, and Hg) were selected to construct 32 antimonene-based SACs. On the pristine antimonene, six transition metal atoms (Mo, Ru, W, Re, Os, Hg) energetically prefer the A site; three transition

metal atoms (Cu, Ag, Au) tend to occupy the B site; and seven transition metal atoms (Fe, Co, Ni, Rh, Pd, Ir, Pt) adopt the C site (Figs. S1-S3). Both steric effect and electronic effect can contribute to the configurations of these SACs. Metals preferring the A site generally have large van der Waals atomic radii in the range of 2.13 to 2.23 Å; since their d orbitals are far from filled (except for Hg), they tend to interact strongly with surrounding Sb atoms, which causes distortions of substrate's geometry. In comparison, metals preferring the C site have small atomic radii in the range of 1.97 to 2.13 Å, and therefore they can be intercalated between two sublayers of Sb atoms. As for metals preferring the B site, they belong to group 11 of the periodic table with the electronic configuration of $d^{10}s^1$, which is relatively inert due to the fully filled dorbitals and half-filled s orbitals. Although Cu, Ag, and Au also have small atomic radii in the range of 1.96 to 2.14 Å, their relatively inert nature keeps them away from the C site that are coordinated by six surrounding Sb atoms. The van der Waals atomic radii are adopted for the above rationalizations because most metals discussed above are proved to be negatively charged, indicating that their atomic radii should be different from those of cationic ions. However, we note that the trend can be still rationalized if the covalent atomic radii are used. On the defective antimonene, all transition metal atoms under study can be trapped in the vacancy (Fig. S4). The 32 antimonene-based SACs are thermodynamically stable, as their binding energies for adsorbing transition metal are all negative (Fig. S5). Due to the passivation of dangling bonds in the point vacancy, all d-M models have more negative binding energies than their p-M counterparts, indicating a stronger interaction between the transition metal atom and the defective antimonene.

Since the electronegativity (χ) only gives a rough estimation of the charge states (Fig. S6), a Bader charge analysis was adopted to confirm the charge states of the 16 metal centers on 32 SACs at the DFT level of theory [85,86]. Fig. 1b shows that 13 transition metal atoms carry negative charge states for both p-M and d-M modes, leading to 26 anionic SACs, while only three transition metals (Fe, Mo, and W) are cationic. The charge states of 3d/4d/5d transition metals exhibit a regular pattern with respect to their atomic number on the periodic table: all three curves are of a V-shape; and the three cationic transition metals are located on the leftmost position of each V-shaped curve, while the transition metals in group 9 (Co, Rh, Ir) have the most negative charges. Most transition metals are more anionic on the pristine antimonene, except for four transition metal atoms (Cu, Ag, Au, and Hg) which are more

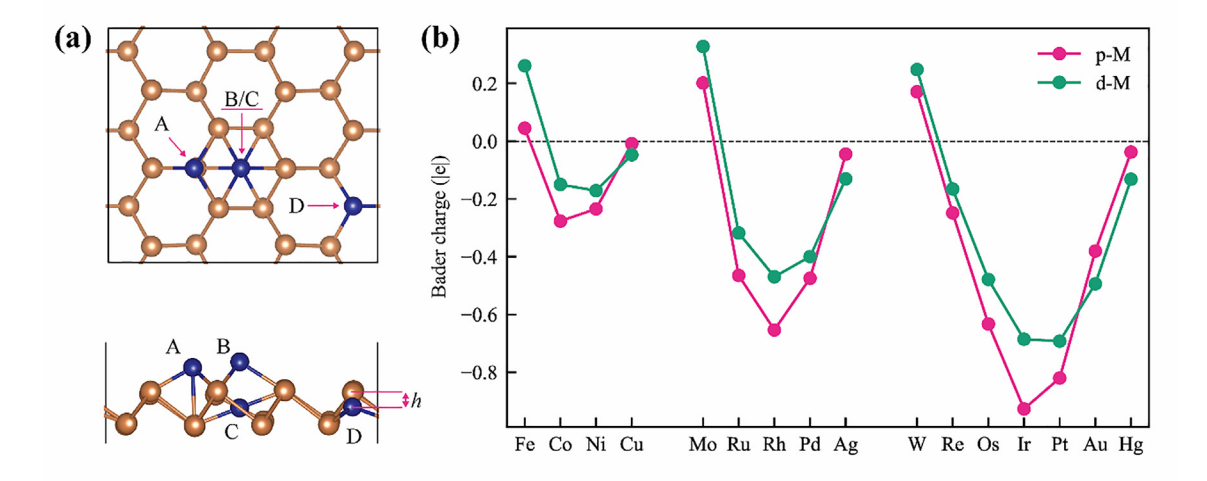


Fig 1. Geometries and charge states of transition metals on antimonene. (a) Schematic of four adsorption sites, where *h* denotes the deviation of a transition metal atom from the top Sb layer. (b) Bader charges of the transition metal (TM) atoms.

anionic on the defective antimonene. Considering that Bader charge analyses in certain cases can yield too extreme values and overestimate the ionic character [87], we also performed a Hirshfeld charge analysis for these SACs (Fig. S7) [88]. Both Bader and Hirshfeld charge analyses confirmed the anionic characteristic for eight metals (Co, Ni, Ru, Rh, Re, Os, Ir, and Pt), which further supports the existence of anionic metal centers and validates our guideline for designing anionic SACs.

3.2. Optimal anionic SACs towards ORR

Before examining the catalytic performance of the 26 anionic SACs towards ORR, we investigated their electronic properties to check if they are suited as potential electrode materials. The pristine antimonene has a theoretical band gap of 1.26 eV (Fig. S8). Dispersing transition metal atoms on the antimonene greatly narrows the band gap: 16 SACs (d-Fe, p-Co, d-Ni, p-Cu, d-Cu, p-Rh, d-Pd, p-Ag, d-Ag, p-Re, d-Re, p-Ir, d-Pt, p-Au, d-Au, and d-Hg) are metallic, as revealed by their density-of-states; the other 10 SACs remain semiconductors, but their band gaps are smaller than 1 eV (Figs. S9–S12). The vanished or reduced band gaps should endow these antimonene-based SACs with enhanced conductivity for electrochemical applications, for instance, as electrocatalysts for ORR

To expedite the screening of optimal electrocatalysts for electrochemical ORR, a three-step strategy was adopted (Fig. 2a). ORR can proceed through a two-electron or a four-electron mechanism. In the two-electron mechanism, O_2 is reduced to H_2O_2 ,

while in the four-electron mechanism, O_2 is reduced to H_2O via dissociative or associative pathways. At step 1 of the screening process, we first evaluated $\Delta G(^*O)$ to discriminate between the two- and four-electron mechanisms, as Guo et al. found that if an electrocatalyst prefers the two-electron mechanism, the value of $\Delta G(^*O)$ is larger than 3.52 eV [89,90]. In the present work, none of the 26 anionic SACs have an $\Delta G(^*O)$ value larger than 3.52 eV (Table S4), indicating that these SACs do not catalyze ORR through the two-electron mechanism. As for the four-electron mechanism, it has dissociative and associative pathways [89]. However, the dissociative pathway is usually not considered for SACs, since breaking the O-O chemical bond requires a large activation energy, and SACs are in lack of contiguous active sites [8,89]. Thus, we only examined the associative pathway of the four-electron mechanism for the 26 anionic SACs.

In the subsequent two steps of the screening process, we evaluated the limiting potential $(U_{\rm L})$ for all the 26 SACs. From separate calculations, the benchmark Pt(111) with an O coverage of 50% presents a $U_{\rm L}$ of 0.64 V towards ORR (Fig. S13). Therefore, the criterion of $U_{\rm L} \geq 0.60$ V was used to find SACs with energy efficiency comparable to Pt(111). The criterion requires $U_{\rm i}^0 \geq 0.60$ V (i = b, c, d, and e) in Eq. (3) according to the definition of $U_{\rm L}$. At step 2 of the screening, $\Delta G(^*{\rm OH})$ was calculated, and with the values of $\Delta G(^*{\rm O})$ from step 1, $U_{\rm d}^0$ and $U_{\rm e}^0$ were determined for each SAC. For qualified electrocatalysts, $U_{\rm d}^0$ and $U_{\rm e}^0$ should be no less than 0.60 V (Fig. 2a). During this process, nineteen anionic SACs were screened out, leaving seven (p-Pd, p-Au, p-Pt, p-Rh, d-Au, p-Co, d-Hg) for further evaluations (Table S4). This step significantly improves the screen-

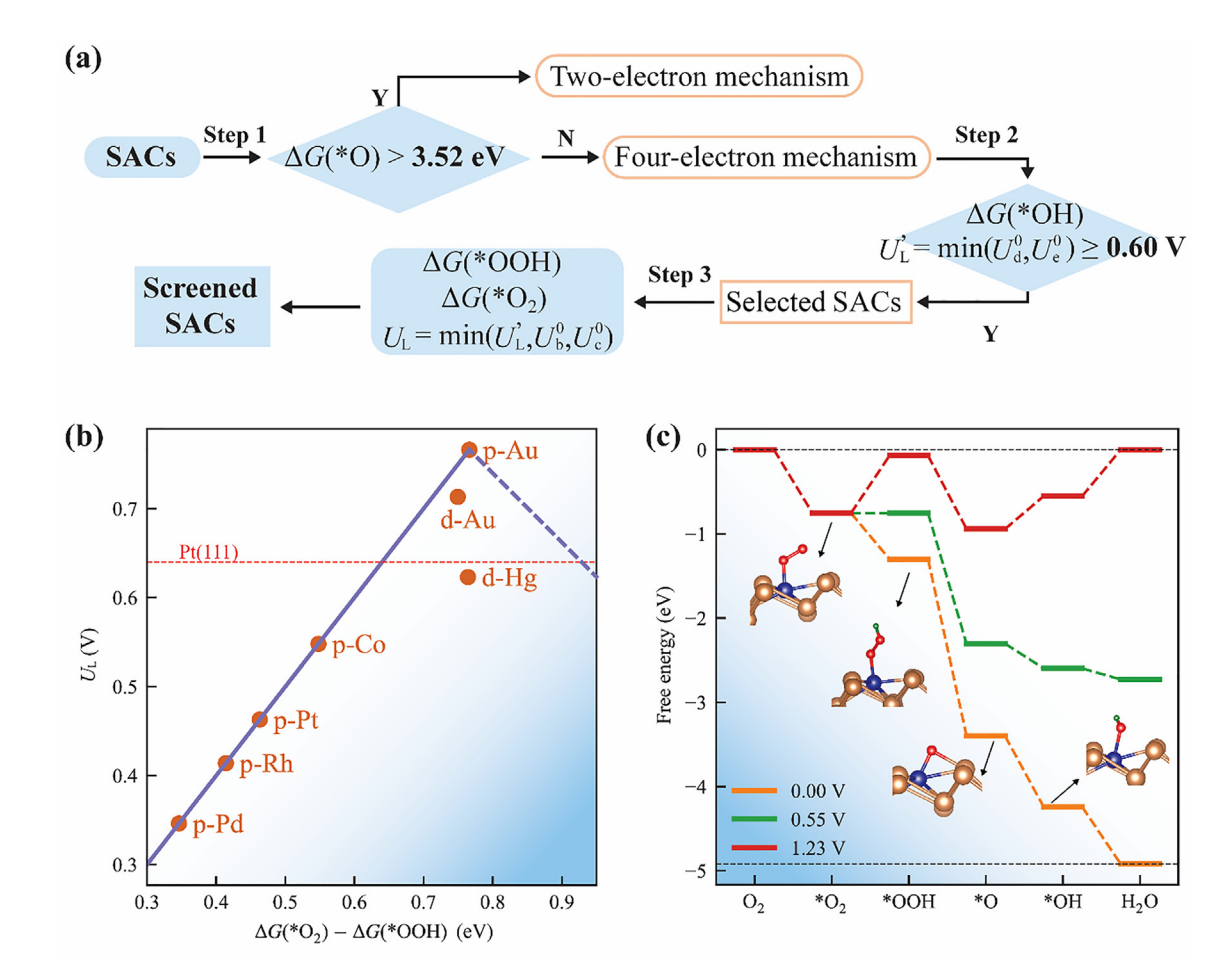


Fig 2. The screening process and results for optimal electrocatalysts to ORR. (a) Three-step strategy. (b) Volcano plot of the limiting potential. The right branch is drawn by hand to show a proposed trend due to the small number of data points. (c) Free energy profile for ORR on p-Co SAC under various external potentials.

ing efficiency of SACs towards ORR, as it excludes 73% anionic SACs. At step 3 of the screening, we further calculated $U_{\rm b}^0$ and $U_{\rm c}^0$ from the values of $\Delta G(^*{\rm O})$, $\Delta G(^*{\rm OOH})$, and $\Delta G(^*{\rm O}_2)$ for the seven catalysts. This finally determines $U_{\rm L}$ of the seven catalysts (Table S5), showing that p-Au, d-Au, and d-Hg are comparable to or even better than Pt(111) in terms of $U_{\rm L}$. Comparing the values of $U_{\rm i}^0$ and $U_{\rm L}$ for the seven candidates, we found that the potential determining step (PDS) is the first protonation step ($^*{\rm O}_2$) *OOH, Eq. (1b)) for five p-M catalysts (M = Au, Co, Pt, Rh, Pd), but is the third protonation step ($^*{\rm O}_3$) *OH, Eq. (1d)) for d-Au, and is the final protonation step ($^*{\rm O}_3$) *OH, Eq. (1e)) for d-Hg. Since Eq. (1b) ($^*{\rm O}_2$) *OOH) is the PDS for most of these catalysts, the value of $\Delta G(^*{\rm O}_2)$ - $\Delta G(^*{\rm OOH})$ can be used as a descriptor to construct the volcano plot (Fig. S14). Fig. 2b shows an approximate volcano shape with p-Au at the peak.

For these anionic SACs to be stable during electrocatalysis, the anion metal centers should remain isolated. Among the seven candidates, we examined p-Au first since it presents the highest U_L in Fig. 2b. For Au atoms on the surface of pristine antimonene, the conformation with one Au-Au dimer is lower in energy than the conformation with isolated Au atoms (Fig. S15a). This suggests that Au atoms on the pristine antimonene tend to form clusters, as reflected by the three-Sb coordination and relatively weak binding energy for p-Au (Figs. S2 and S5). Likewise, d-Hg has a weak binding energy. In contrast, the other five candidates (p-Co, p-Pt, p-Rh, p-Pd, and d-Au) can remain as isolated transition metals, because the binding energies of these SACs are much stronger (-3.81, -5.45, -5.51, -3.77, and -4.10 eV, respectively). These strong binding energies can be ascribed to their stable conformations where Co, Pt, Rh, and Pd atoms are deeply embedded inside the Sb buckled hexagonal ring while Au atom in d-Au occupies the Sb-vacancy, and therefore are firmly locked by the six coordinating Sb atoms or the three chemical bonds (Figs. S3 and S4). Accordingly, Co, Pt, Rh, and Pd atoms hardly diffuse on the surface as these atoms are much more stable inside the hexagonal ring than on the surface (Fig. S15b-d), which hinders the clustering. By excluding p-Au and d-Hg, the best catalyst for ORR is d-Au with a U_L of 0.71 V.

Among the seven catalysts, p-Co is the only noble metal-free catalyst, and thus attracts our attention. The U_L of p-Co is around 0.55 V which ranks the highest among the stable p-M (M = Co, Pt, Rh, and Pd) catalysts and is close to that of Pt(111). Fig. 2c shows the free energy profiles of p-Co under external potentials. The O₂ molecule can be strongly adsorbed on the anionic Co center, causing the first protonation step to be the PDS which presents a free energy change about -0.55 eV. The insets in Fig. 2c also shows a Sb-O bond in *O intermediate, suggesting a synergy interaction between the transition metal and the adjacent atom. The discovery of p-Co provides another method to improve the ORR activity of Co [91], besides developing N-coordinated Co SACs [91–93]. For comparison, we further constructed graphene-based cationic CoN₄ SACs (Fig. S16) and examined the catalytic performance towards ORR. The Co metal center on Sb-based anionic SAC carries a charge state of -0.27 |e|, while that on CoN₄ cationic SACs carries a charge state of + 0.91 |e|. The CoN₄ cationic SAC exhibits a U_L of only 0.36 V for the same PDS step (Fig. S17), which is compatible with previously reported values [94,95] but much smaller than the $U_{\rm L}$ of 0.55 eV for p-Co anionic SAC. Since the CoN₄ cationic SAC was reported to display outstanding catalytic performance toward ORR [93], we believe the anionic SACs presented in this work call for more attention.

3.3. Origin of ORR activity on anionic Co

The origin of ORR activity on anionic Co was evaluated firstly by comparing the adsorption and activation processes of O₂ molecule

on p-Co and CoN₄ SACs, since these processes are crucial for ORR [96]. When an O_2 molecule stays away from the p-Co and CoN_4 , the density-of-states (DOS) peaks are apparently derived from its molecular orbitals (Fig. 3a). After the chemisorption, the σ and π^* DOS peaks of O_2 on p-Co and CoN_4 vanish, indicating d- σ and d- π^* interactions. This finding confirms the activation of the O₂ molecule on both kinds of metal centers. The activation process consists of two simultaneous steps: O2 forms bonds with the metal center via bonding orbitals of O_2 and d orbitals of the metal, then the metal center donates electrons from its d orbitals back to the antibonding orbitals of O_2 . For the cationic Co center, the π DOS peaks of O₂ also disappear after the adsorption, because cationic metal centers usually present more vacant d orbitals which are ready for a d- π interaction. The additional d- π interaction implies a more negative adsorption energy of O₂ on cationic metal centers than their anionic counterparts, which is confirmed by our calculation as shown in Fig. 3b. The weaker adsorption of O₂ on anionic p-Co SACs can also be partially ascribed to the steric effect: Co in p-Co is located between two Sb sublayers (Fig. S3), which may cause a penalty of repulsion due to the short distance between O2 and the top Sb sublayer. Nevertheless, the anionic metal centers show a more intensive activation effect on the O₂ molecule. The anionic Co center in p-Co overall transfers 0.66 electrons to the adsorbed O₂ molecule, more than its cationic counterpart CoN₄ (0.39 electrons). As a result, O₂ on an anionic metal center exhibits longer O-O bond length (1.34 Å) than on cationic metal centers (1.31 Å). Therefore, anionic metal centers can better promote the activation of O₂, thus being significant to many reactions, such as the CO oxidation reaction [40].

In stark contrast to the case of O_2 adsorption that is weaker on the anionic Co, the anionic Co binds *OOH, *O, and *OH intermediates more strongly than its cationic counterpart. Fig. 3b shows that the adsorption free energies of *OOH, *O, and *OH on anionic Co are less positive than those on the cationic counterpart. In other words, the anionic metal center helps to stabilize the reaction intermediates. This stabilization effect is the most pronounced for the *O intermediate. Therefore, the stabilization effect of anionic metal centers can favorably tune the ORR activity. As a matter of fact, the weaker adsorption of the *O₂ intermediate and the stronger adsorption of the *OOH intermediate directly contribute to the larger U_L of the anionic p-Co (0.55 V) than the cationic CoN₄ catalyst (0.36 V) found in the previous section.

3.4. Anionic SACs for electrochemical reactions beyond ORR

Due to the strong electron-donating property of anionic metal centers, we then explored their potentials to catalyze other electrochemical reactions, for example, nitrogen reduction reaction (NRR). For NRR, the stepped Ru(0001) is recognized as the most promising metal electrocatalyst [97], with the highest U_L (ca. -0.43 V) among bulk metals (Fig. S18). The challenge of developing effective electrocatalysts for NRR is that N2 is very stable and the electrochemical reduction of N2 requires active centers with ability to strongly adsorb intermediates. When screening ORR catalysts, we noticed that three anionic SACs (d-Ru, d-Os, and d-Re) present very strong adsorption to oxygen-containing intermediates, as reflected by their negative values of $\Delta G(^*OH)$ (Table S4). Thus, d-Ru, d-Os, and d-Re were selected as candidates of NRR catalyst. By setting the stepped Ru(0001) as a benchmark, anionic SACs among d-Ru, d-Os, and d-Re with a U_L close to or less negative than -0.43 V is demanded. Since NRR can proceed via many mechanisms such as enzymatic, distal, and alternating mechanisms (Scheme S1), a thorough screening process was established by starting with the evaluation of N₂ adsorption on the metal centers of SACs.

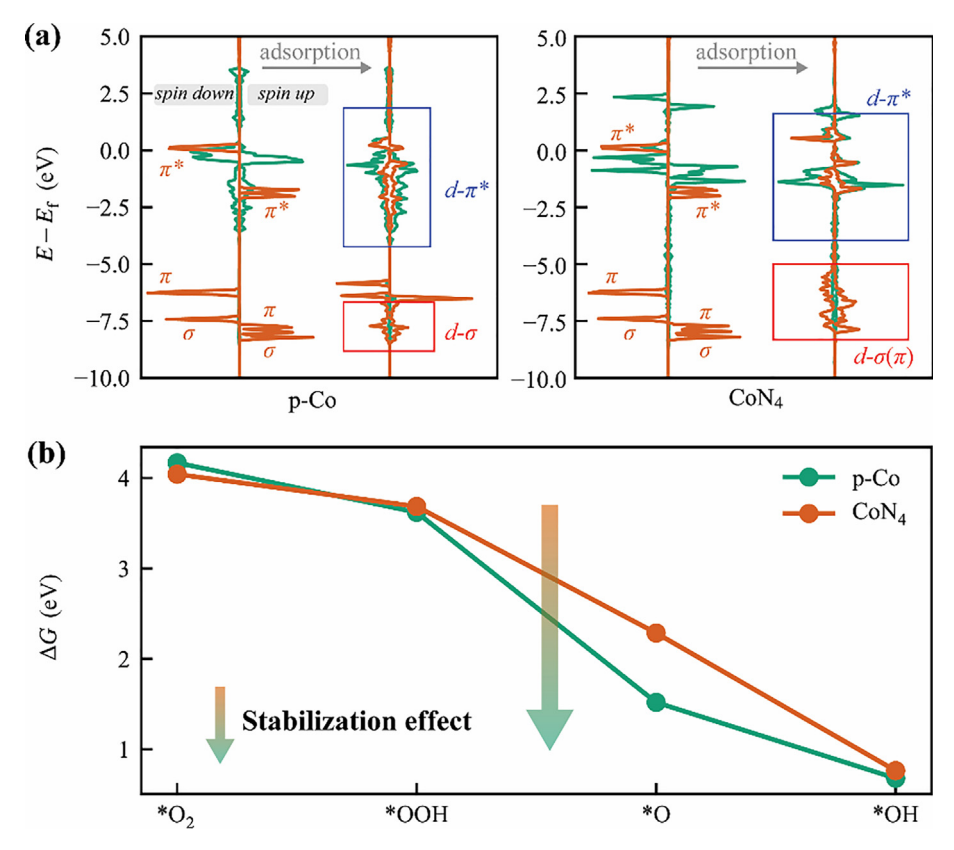


Fig 3. Activation of O_2 and adsorption of oxygen-containing species. (a) DOS of O_2 on p-Co and CoN₄ surfaces, where orange curves represent DOS for O_2 , and green curves represent DOS for the d orbitals of Co. (b) Adsorption free energies of *O_2 , *OOH , *O , and *OH on Co SACs.

According to our calculations, d-Ru, d-Os, and d-Re prefer to binding N_2 molecule via an end-on mode with ΔE of -1.00, -1.27 and -1.72 eV, respectively (Table S6). After free energy corrections, the corresponding ΔG are -0.43, -0.69, and -1.13 eV (Fig. 4a). In addition, N-N bond lengths are 1.140, 1.147, and 1.157 Å for N₂ adsorbed on d-Ru, d-Os, and d-Re, respectively (Fig. 4b), which are all longer than the bond length of free N₂ molecule (1.11–1.1 2 Å) [98,99]. The negative ΔG and elongated N-N bond lengths indicate that anionic SACs are promising in capturing and activating N₂ molecule. The end-on mode of N₂ adsorption on the three anionic SACs rules out the enzymatic mechanism, leaving only the distal or the alternating mechanism for further considerations. The two mechanisms share one common reduction step, i.e., the reduction of adsorbed *N2 to *N2H, where * represents the active site. In fact, this step turned out to be the PDS of NRR for the SACs under study (vide infra). Therefore, the free energy change from *N₂ to *N₂H, namely $\Delta G(*N_2 \rightarrow *N_2 H)$, can be used to narrow down the number of catalyst candidates. The $\Delta G(^*N_2 \rightarrow ^*N_2H)$ for d-Ru, d-Os, and d-Re were calculated to be 0.62, 0.41, and 0.46 eV, respectively (Table S6). As a result, d-Os and d-Re were selected for further study, because their $\Delta G(^*N_2 \rightarrow ^*N_2H)$ are comparable to the Ru(0001) benchmark. The *N₂H intermediate on d-Os and d-Re anionic SACs can either become *N2H2 or *NHNH, depending on which N atom the H⁺/e⁻ pair attacks. A *N₂H₂ intermediate leads to a distal mechanism, while a *NHNH intermediate proceeds through an alternating mechanism. By comparing the energy between *N₂H₂ and *NHNH for d-Os and d-Re, we confirmed that the *N₂H intermediate tends to form *N₂H₂ intermediate on the two candidates (Fig. S19). Thus, d-Os and d-Re prefer catalyzing NRR via the distal mechanism and the corresponding downstream intermediates are *N, *NH, *NH2, and *NH3.

Fig. 4c and d shows the free energy profiles for NRR on d-Os and d-Re, respectively. The PDS steps for d-Os and d-Re are the

same, i.e., the conversion of *N_2 to *N_2H , corresponding to U_L of -0.41, and -0.46 V, respectively. Therefore, the d-Os is the best electrocatalyst for NRR revealed in this work. For comparison, we also examined the NRR performance of graphene-based OsN₄ and ReN₄ SACs (Fig. S20). As can be seen from Fig. 4c and d, OsN_4 and ReN_4 show U_L values of -0.76 and -0.57 V towards NRR, which are inferior to their anionic counterparts. Here, the stabilization effect of anionic metal centers on various intermediates is playing an important role to increase the energy efficiency. It is noteworthy that the anionic Os center can stabilize five intermediates compared with the cationic Os center (Fig. 4c). The stabilization effect also has significant impacts on the PDS of NRR. For d-Os/OsN₄, the stabilization effect reduces the energy barrier of PDS from 0.76 to 0.41 eV. From ReN₄ to d-Re, the stabilization effect even changes the PDS from the last proton/electron step (*NH₂→*NH₃) to the first proton/electron step (*N₂→*N₂H). These results demonstrate the advantage of anionic SACs for electrocatalysis of NRR.

Considering that the standard GGA tends to underestimate the band gaps, we also used the Heyd-Scuseria-Ernzerhof (HSE06) [100] hybrid functional, which was proven to be very reliable in calculating the electronic properties, to evaluate the band gap values of antimonene and the best screened catalysts for ORR and NRR, namely d-Au, p-Co, d-Os, and d-Re (Table S7). As expected, the band gap values obtained by HSE06 are larger than those obtained by PBE. For the pristine antimonene, the band gap increases from 1.26 eV at PBE to 1.77 eV at HSE06, and these band gaps are consistent with previous studies [101]. For the antimonene-based SACs studied here, both PBE and HSE06 computations show that these screened catalysts have smaller band gaps than the pristine antimonene, especially the HSE06 band gap values for these four antimonene-based SACs are in an acceptable range for electrocatalysts.

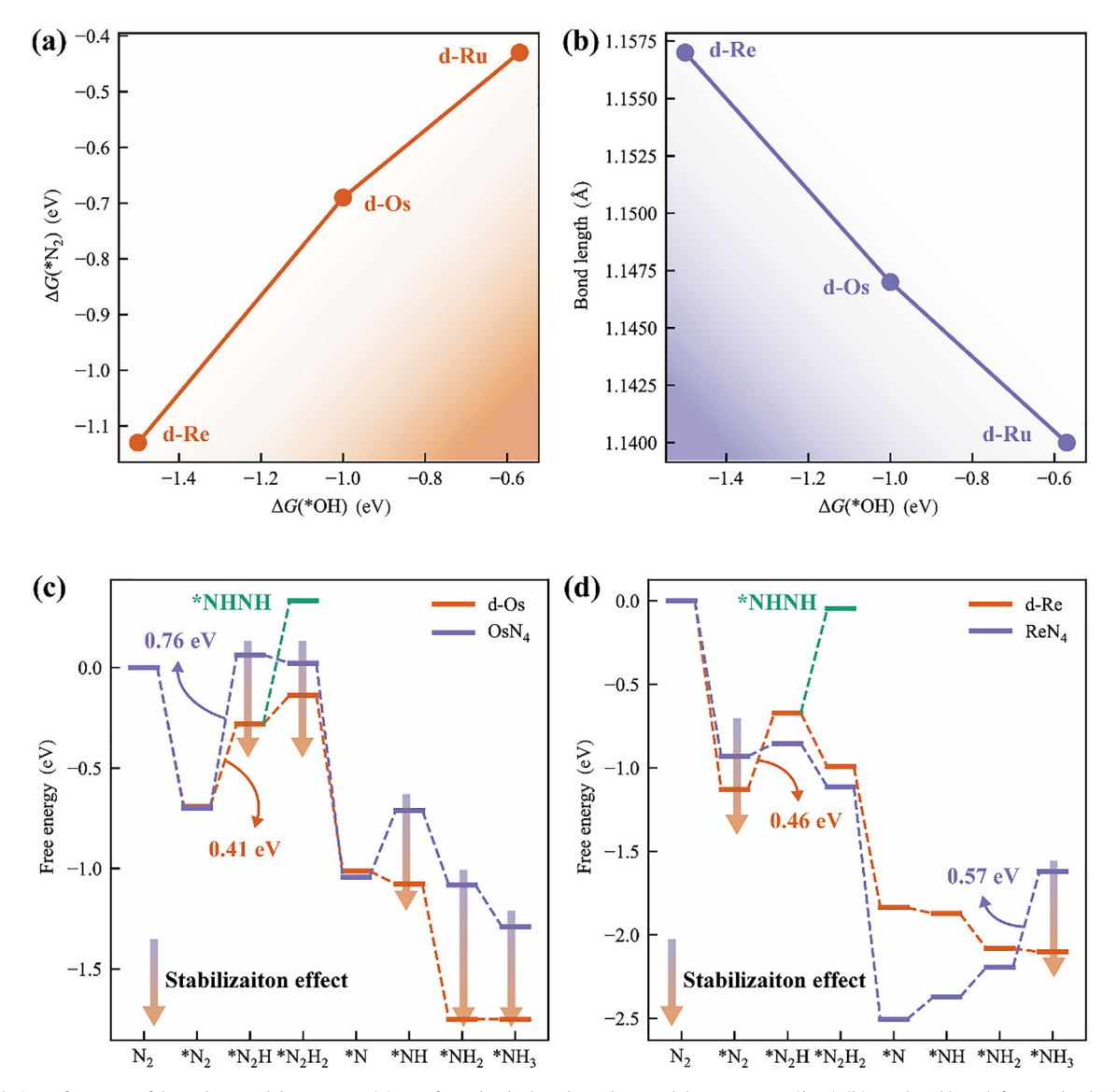


Fig 4. Catalytic performance of d-Ru, d-Os, and d-Re to NRR. (a) ΔG of N₂ adsorbed on d-Ru, d-Os, and d-Re versus $\Delta G(^*OH)$. (b) N-N bond length for N₂ adsorbed on the metal centers versus $\Delta G(^*OH)$. (c and d) Free energy profiles for NRR on d-Os/OsN₄ and d-Re/ReN₄, respectively, where the energy barrier of PDS is labeled, and the stabilization effect is indicated. Calculations were done for the distal mechanism since the alternating mechanism is energetically unfavorable as indicated by the *N_2H_2 step.

4. Conclusions

To achieve single-atom catalysts (SACs) with anionic metal centers, namely anionic SACs, we have proposed in this work a simple guideline based on Pauling electronegativity: the metal centers should have larger electronegativity than the surrounding atoms from the substrate on which the single metal atoms are supported. Following this principle, we have discovered that 13 transition metal atoms (Co, Ni, Cu, Ru, Rh, Pd, Ag, Re, Os, Ir, Pt, Au, and Hg) deposited on pristine or defective antimonene carry anionic charges by means of density functional theory (DFT) simulations. These anionic SACs are promising electrocatalysts for many significant reactions, such as oxygen reduction reaction (ORR) and nitrogen reduction reaction (NRR). For ORR applications, the anionic metal centers can promote the activation of O2 and stabilize the adsorptions of downstream intermediates. From our results, anionic d-Au shows better ORR energy efficiency than the benchmark Pt(111). Another promising electrocatalyst towards ORR is p-Co, due to its high limiting potential and non-precious non-toxic nature. For NRR applications, the d-Os and d-Re electrocatalysts have limiting potentials of -0.41 and -0.46 V, respectively, very close to the stepped Ru(0001) surface. We have further discovered that several transition metal atoms (Os, Ir, Pt, Au) on bismuthene are also anionic (Fig. S21) [58,101]. Such bismuthene-based anionic SACs may also have a promise as electrocatalysts, for example for the electrochemical reduction of $\rm CO_2$ [102]. Overall, this work proposes a guideline for fast design of anionic SACs and provides evidence to utilize anionic SACs as efficient electrocatalysts towards ORR and other important reactions beyond ORR.

Declaration of Competing Interest

The authors declare that they have no known competing financial interests or personal relationships that could have appeared to influence the work reported in this paper.

Acknowledgments

This work was financially supported by the National Science Foundation-Centers of Research Excellence in Science and Technology (NSF-CREST Center) for Innovation, Research and Education in Environmental Nanotechnology (CIRE2N) (Grant No. HRD- 1736093) and the NSF Center for the Advancement of Wearable Technologies (Grant No. 1849243). Some of the work was performed at the Center for Nanophase Materials Sciences, a U.S. DOE Office of Science User Facility. Calculations used the resources of the National Energy Research Scientific Computing Center, which is supported by the Office of Science of the U.S. DOE under Contract No. DE-AC02-05CH11231.

Appendix A. Supplementary data

Supplementary data to this article can be found online at https://doi.org/10.1016/j.jechem.2021.08.004.

References

- [1] J. Guo, X. Zhang, F. Gu, H. Zhang, Y. Fan, J. Clean. Prod. 249 (2020) 119372.
- [2] F. Johnsson, J. Kjärstad, J. Rootzén, Clim. Policy 19 (2019) 258–274.
- [3] L. Du, V. Prabhakaran, X. Xie, S. Park, Y. Wang, Y. Shao, Adv. Mater. 33 (2021) 1908232.
- [4] J.M. Thomas, P.P. Edwards, P.J. Dobson, G.P. Owen, J. Energy Chem. 51 (2020) 405-415.
- [5] X. Tian, X.F. Lu, B.Y. Xia, X.W. Lou, Joule 4 (2020) 45-68.
- [6] K. Kodama, T. Nagai, A. Kuwaki, R. Jinnouchi, Y. Morimoto, Nat. Nanotech. 16 (2021) 140-147.
- [7] D. Liu, L. Tao, D. Yan, Y. Zou, S. Wang, ChemElectroChem 5 (2018) 1775–1785.
- [8] A. Kulkarni, S. Siahrostami, A. Patel, J.K. Nørskov, Chem. Rev. 118 (2018) 2302-2312.
- T. Asset, R. Chattot, M. Fontana, B. Mercier-Guyon, N. Job, L. Dubau, F. Maillard, ChemPhysChem 19 (2018) 1552-1567.
- [10] H. Yuan, Q. Zhang, J. Energy Chem. 48 (2020) 107-108.
- [11] N. Alonso-Vante, Y. Feng, H. Yang, Catalysts 9 (2019) 731.
 [12] X. Tian, X. Zhao, Y.-Q. Su, L. Wang, H. Wang, D. Dang, B. Chi, H. Liu, E.J.M. Hensen, X.W. Lou, B.Y. Xia, Science 366 (2019) 850–856.
 [13] J. Stacy, Y.N. Regmi, B. Leonard, M. Fan, Renew. Sust. Energy Rev. 69 (2017)
- 401-414
- [14] X. Wang, Z. Li, Y. Qu, T. Yuan, W. Wang, Y. Wu, Y. Li, Chem 5 (2019) 1486-1511.
- [15] Y. Li, Q. Li, H. Wang, L. Zhang, D.P. Wilkinson, J. Zhang, Electrochem. Energ. Rev. 2 (2019) 518-538.
- [16] J. Gu, S. Magagula, J. Zhao, Z. Chen, Small Methods 3 (2019) 1800550.
- [17] Y. Li, Y. Tong, F. Peng, J. Energy Chem. 48 (2020) 308–321.
- [18] M. Chen, Y. He, J.S. Spendelow, G. Wu, ACS Energy Lett. 4 (2019) 1619–1633.
- [19] U. Martinez, S.K. Babu, E.F. Holby, H.T. Chung, X. Yin, P. Zelenay, Adv. Mater. 31 (2019) 1806545.
- [20] X. Jiang, J. Chen, F. Lyu, C. Cheng, Q. Zhong, X. Wang, A. Mahsud, L. Zhang, Q. Zhang, J. Energy Chem. 59 (2021) 482-491.
- [21] R. Wang, Y. Yang, Y. Zhao, L. Yang, P. Yin, J. Mao, T. Ling, J. Energy Chem. 58 (2021) 629-635.
- V. Fung, G. Hu, B. Sumpter, J. Mater. Chem. A 8 (2020) 6057-6066.
- [23] N. Cheng, L. Zhang, K. Doyle-Davis, X. Sun, Electrochem. Energy Rev. 2 (2019) 539-573.
- B. Singh, V. Sharma, R.P. Gaikwad, P. Fornasiero, R. Zbořil, M.B. Gawande, Small 17 (2021) 2006473.
- [25] M.B. Gawande, P. Fornasiero, R. Zbořil, ACS Catal. 10 (2020) 2231-2259.
- [26] H. Li, H. Zhu, Z. Zhuang, S. Lu, F. Duan, M. Du, Sustain. Energy Fules 4 (2020) 996-1011.
- [27] X.-F. Yang, A. Wang, B. Qiao, J. Li, J. Liu, T. Zhang, Acc. Chem. Res. 46 (2013) 1740-1748.
- [28] A. Wang, J. Li, T. Zhang, Nat. Rev. Chem. 2 (2018) 65-81.
- [29] J. Kim, H.-E. Kim, H. Lee, ChemSusChem 11 (2018) 104-113.
- [30] L. Liu, A. Corma, Chem. Rev. 118 (2018) 4981-5079.
- [31] H. Zhang, G. Liu, L. Shi, J. Ye, Adv. Energy Mater. 8 (2018) 1701343.
- [32] N. Daelman, M. Capdevila-Cortada, N. López, Nat. Mater. 18 (2019) 1215-
- [33] R. Lang, T. Li, D. Matsumura, S. Miao, Y. Ren, Y.-T. Cui, Y. Tan, B. Qiao, L. Li, A. Wang, X. Wang, T. Zhang, Angew. Chem. Int. Ed. Engl. 55 (2016) 16054-
- [34] Y. Han, Y. Wang, R. Xu, W. Chen, L. Zheng, A. Han, Y. Zhu, J. Zhang, H. Zhang, J. Luo, C. Chen, Q. Peng, D. Wang, Y. Li, Energy Environ. Sci. 11 (2018) 2348-
- [35] J.E. Ellis, Inorg. Chem. 45 (2006) 3167-3186.
- [36] R. Sloane, H. Love, Nature 159 (1947) 302-303.
- [37] W. Spicer, A. Sommer, J. White, Phys. Rev. 115 (1959) 57-62.
- [38] C. Goodman, J. Phys. Chem. Solids 6 (1958) 305–314.
- [39] X. Zhou, Q. Shen, K. Yuan, W. Yang, Q. Chen, Z. Geng, J. Zhang, X. Shao, W. Chen, G. Xu, J. Am. Chem. Soc. 140 (2018) 554-557.
- [40] T. Kropp, Z. Lu, Z. Li, Y.-H.-C. Chin, M. Mavrikakis, ACS Catal. 9 (2019) 1595-
- [41] A.P. Woodham, G. Meijer, A. Fielicke, Angew. Chem. Int. Ed. Engl. 51 (2012) 4444-4447.

- [42] H. Zhang, T. Watanabe, M. Okumura, M. Haruta, N. Toshima, Nat. Mater. 11 (2012)49-52
- [43] A.S. Nair, B. Pathak, J. Phys. Chem. C 123 (2019) 3634-3644.
- [44] A. Laghrissi, M. Es-Souni, Catal, Sci. Technol. 9 (2019) 4355-4364.
- [45] J. Wu, S. Shan, H. Cronk, F. Chang, H. Kareem, Y. Zhao, J. Luo, V. Petkov, C.-J. Zhong, J. Phys. Chem. C 121 (2017) 14128-14136.
- [46] S. Tymen, A. Undisz, M. Rettenmayr, A. Ignaszak, J. Mater. Research 30 (2015) 2327-2339.
- [47] P. Balbuena, R. Callejas-Tovar, P.d. Hirunsit, J.M. De La Hoz, Y. Ma, Topics Catal 55 (2012) 322-335
- [48] Y. Ma, P.B. Balbuena, J. Electrochem. Soc. 157 (2010) B959-B963.
- [49] H. Li, G. Sun, N. Li, S. Sun, D. Su, Q. Xin, J. Phys. Chem. C 111 (2007) 5605-
- [50] S.-I. Choi, S. Xie, M. Shao, J.H. Odell, N. Lu, H.-C. Peng, L. Protsailo, S. Guerrero, J. Park, X. Xia, Nano Lett. 13 (2013) 3420-3425.
- [51] C.T. Campbell, Nat. Chem. 4 (2012) 597-598.
- [52] C. Ling, Y. Ouyang, Q. Li, X. Bai, X. Mao, A. Du, J. Wang, Small Methods 3 (2019) 1800376
- [53] Z. Chen, J. Zhao, C.R. Cabrera, Z. Chen, Small Methods 3 (2019) 1800368.
- [54] S. Zhang, Z. Yan, Y. Li, Z. Chen, H. Zeng, Angew. Chem. Int. Ed. Engl. 54 (2015) 3112-3115.
- [55] P. Ares, F. Aguilar-Galindo, D. Rodríguez-San-Miguel, D.A. Aldave, S. Díaz-Tendero, M. Alcamí, F. Martín, J. Gómez-Herrero, F. Zamora, Adv. Mater. 28 (2016) 6332-6336.
- [56] C. Gibaja, D. Rodriguez-San-Miguel, P. Ares, J. Gómez-Herrero, M. Varela, R. Gillen, J. Maultzsch, F. Hauke, A. Hirsch, G. Abellán, Angew. Chem. Int. Ed. Engl. 55 (2016) 14345-14349.
- [57] J. Ji, X. Song, J. Liu, Z. Yan, C. Huo, S. Zhang, M. Su, L. Liao, W. Wang, Z. Ni, Nat. Commun. 7 (2016) 13352.
- [58] M. Pumera, Z. Sofer, Adv. Mater. 29 (2017) 1605299.
- [59] L. Yang, Y. Song, W. Mi, X. Wang, Appl. Phys. Lett. 109 (2016) 022103.
- [60] Y. Zhang, M. Qiao, Y. Huang, Y. Zou, Z. Liu, L. Tao, Y. Li, C.-L. Dong, S. Wang, Research 2020 (2020) 5487237.
- [61] R. Gusmão, Z. Sofer, D. Bouša, M. Pumera, Angew. Chem. Int. Ed. Engl. 56 (2017) 14417-14422.
- [62] X. Ren, Z. Li, H. Qiao, W. Liang, H. Liu, F. Zhang, X. Qi, Y. Liu, Z. Huang, D. Zhang, J. Li, J. Zhong, H. Zhang, A.C.S. Appl, Energy Mater. 2 (2019) 4774–4781.
- Y. Hu, J. Sun, H. Wei, M. Ai, Z. Li, New J. Chem. 44 (2020) 1138–1146.
- [64] S. Lu, H.L. Huynh, F. Iou, K. Guo, Z. Yu, Nanoscale 13 (2021) 12885-12895.
- [65] G. Kresse, J. Furthmüller, Comput. Mater. Sci. 6 (1996) 15–50.
- [66] G. Kresse, J. Furthmüller, Phys. Rev. B 54 (1996) 11169–11186. [67] J.P. Perdew, K. Burke, M. Ernzerhof, Phys. Rev. Lett. 77 (1996) 3865–3868.
- [68] P.E. Blöchl, Phys. Rev. B 50 (1994) 17953-17979.
- [69] G. Kresse, D. Joubert, Phys. Rev. B 59 (1999) 1758-1775.
- [70] H.J. Monkhorst, J.D. Pack, Phys. Rev. B 13 (1976) 5188–5192.
- [71] S. Ren, Q. Yu, X. Yu, P. Rong, L. Jiang, J. Jiang, Sci. China Mater. 63 (2020) 903-
- [72] W.L. Wang, E.J.G. Santos, B. Jiang, E.D. Cubuk, C. Ophus, A. Centeno, A. Pesquera, A. Zurutuza, J. Ciston, R. Westervelt, E. Kaxiras, Nano Lett. 14 (2014) 450-455.
- [73] P. Serp, P. Kalck, R. Feurer, Chem. Rev. 102 (2002) 3085-3128.
- [74] H. Yan, H. Cheng, H. Yi, Y. Lin, T. Yao, C. Wang, J. Li, S. Wei, J. Lu, J. Am. Chem. Soc. 137 (2015) 10484-10487.
- [75] S. Sun, G. Zhang, N. Gauquelin, N. Chen, J. Zhou, S. Yang, W. Chen, X. Meng, D. Geng, M.N. Banis, R. Li, S. Ye, S. Knights, G.A. Botton, T.-K. Sham, X. Sun, Sci. Rep. 3 (2013) 1775.
- [76] S. Liu, M. Wang, X. Yang, Q. Shi, Z. Qiao, M. Lucero, Q. Ma, K.L. More, D.A. Cullen, Z. Feng, G. Wu, Angew. Chem. Int. Ed. Engl. 59 (2020) 21698-21705.
- [77] S. Grimme, J. Antony, S. Ehrlich, H. Krieg, J. Chem. Phys. 132 (2010) 154104. [78] K. Mathew, V.C. Kolluru, S. Mula, S.N. Steinmann, R.G. Hennig, J. Chem. Phys. 151 (2019) 234101.
- [79] K. Mathew, R. Sundararaman, K. Letchworth-Weaver, T.A. Arias, R.G. Hennig, J. Chem. Phys. 140 (2014) 084106.
 [80] J.K. Nørskov, J. Rossmeisl, A. Logadottir, L. Lindqvist, J.R. Kitchin, T. Bligaard, H. 17803 (17803) 17806 (17803) Jonsson, J. Phys. Chem. B 108 (2004) 17886–17892.
- [81] W. Liang, J. Chen, Y. Liu, S. Chen, ACS Catal. 4 (2014) 4170–4177.
- [82] J. Liu, M. Yu, X. Wang, J. Wu, C. Wang, L. Zheng, D. Yang, H. Liu, Y. Yao, F. Lu, J. Mater. Chem. A 5 (2017) 20922-20931.
- [83] J. Zhao, C.R. Cabrera, Z. Xia, Z. Chen, Carbon 104 (2016) 56-63.
- [84] V. Wang, N. Xu, J.-C. Liu, G. Tang, W.-T. Geng, Comput. Phys. Comm. 267 (2021) 108033.
- [85] G. Henkelman, A. Arnaldsson, H. Jónsson, Comput. Mater. Sci. 36 (2006) 354-360.
- [86] M. Yu, D.R. Trinkle, J. Chem. Phys. 134 (2011) 064111.
- [87] C.F. Guerra, J.W. Handgraaf, E.J. Baerends, F.M. Bickelhaupt, J. Comput. Chem. 25 (2004) 189-210.
- [88] F.L. Hirshfeld, Theor. Chim. Acta 44 (1977) 129-138.
- [89] X. Guo, S. Lin, J. Gu, S. Zhang, Z. Chen, S. Huang, ACS Catal. 9 (2019) 11042-11054
- [90] Y. Wang, Z. Zhang, X. Zhang, Y. Yuan, Z. Jiang, H. Zheng, Y.-G. Wang, H. Zhou, Y. Liang, CCS Chem. 3 (2021) 585–593.
- [91] Y. He, S. Hwang, D.A. Cullen, M.A. Uddin, L. Langhorst, B. Li, S. Karakalos, A.J. Kropf, E.C. Wegener, J. Sokolowski, Energy Environ. Sci. 12 (2019) 250-260.
- [92] P. Yin, T. Yao, Y. Wu, L. Zheng, Y. Lin, W. Liu, H. Ju, J. Zhu, X. Hong, Z. Deng, Angew. Chem. Int. Ed. Engl. 55 (2016) 10800–10805.

- [93] Q. Yang, Y. Jia, F. Wei, L. Zhuang, D. Yang, J. Liu, X. Wang, S. Lin, P. Yuan, X. Yao, Angew. Chem. Int. Ed. Engl. 132 (2020) 6178–6183.
 [94] J. Zhang, J. Yang, Y. Wang, H. Lu, M. Zhang, Int. J. Energy Res. 45 (2021) 10858–
- 10868.
- [95] F. Wu, C. Pan, C.-T. He, Y. Han, W. Ma, H. Wei, W. Ji, W. Chen, J. Mao, P. Yu, D. Wang, L. Mao, Y. Li, J. Am. Chem. Soc. 142 (2020) 16861–16867.
 [96] E.I. Solomon, S.S. Stahl, Chem. Rev. 118 (2018) 2299–2301.
- [97] E. Skulason, T. Bligaard, S. Gudmundsdóttir, F. Studt, J. Rossmeisl, F. Abild-Pedersen, T. Vegge, H. Jonsson, J.K. Nørskov, Phys. Chem. Chem. Phys. 14 (2012) 1235–1245.
- [98] X. Guo, J. Gu, S. Lin, S. Zhang, Z. Chen, S. Huang, J. Am. Chem. Soc. 142 (2020) 5709–5721.
- [99] Y.-H. Tian, S. Hu, X. Sheng, Y. Duan, J. Jakowski, B.G. Sumpter, J. Huang, J. Phys. Chem. Lett. 9 (2018) 570–576.
- [100] J. Heyd, G.E. Scuseria, M. Ernzerhof, J. Chem. Phys. 118 (2003) 8207–8215.
 [101] S. Zhang, S. Guo, Z. Chen, Y. Wang, H. Gao, J. Gómez-Herrero, P. Ares, F. Zamora, Z. Zhu, H. Zeng, Chem. Soc. Rev. 47 (2018) 982–1021.
- [102] F. Yang, A.O. Elnabawy, R. Schimmenti, P. Song, J. Wang, Z. Peng, S. Yao, R. Deng, S. Song, Y. Lin, M. Mavrikakis, W. Xu, Nat. Commun. 11 (2020) 1088.